TURBULENT FLOW SIMULATIONS ABOUT THE AIRCRAFT CONFIGURATION

Yoonsik Kim[1], Soo Hyung Park[2], Jang-Hyuk Kwon*[3]

항공기 주위 난류 유동장 해석

김 윤 식[1], 박 수 형[2], 권 장 혁*[3]

An application of the KFLOW3D code which has been developed at KAIST is presented. This paper briefly describes the underlying methodology and summarizes the results for the DLR-F6 transport configuration recently presented in the second AIAA CFD Drag Prediction Workshop held in Orlando, FL, June 2003. KFLOW3D is a parallelized Reynolds averaged Navier-Stokes solver for multi-block structured grids. For the present computations, 2-equation k-ω WD+ nonlinear eddy viscosity model is used. The emphasis of the paper is placed on the implementation of the k-ω WD+ model in the multigrid framework and practicality of KFLOW3D for accurately predicting not only the integrated aerodynamic property such as the drag coefficient but pressure distributions.

Key Words: Turbulent Flow Simulation, Multigrid, k-ω WD+ Turbulent model, Drag Prediction, Grid Convergence Study

1. INTRODUCTION

The computational fluid dynamics(CFD) has been developed enough to be applied for practical aircraft configurations. However, the turbulent flow analysis of 3-dimensional configuration often takes a prohibitively large computing time or ends up with an unreliable solution due to inaccuracies in applied methods. The robust CFD code can be routinely used to predict aircraft force coefficients such as lift, drag and moments, as well as the changes in these values with design changes. The robustness of a particular CFD code must be assessed by undergoing extensive verification including the determination of adequate grid resolution prior to being trusted as a useful predictive tool. With these issues in mind, the AIAA Applied Aerodynamics technical committee organized a Drag Prediction Workshop, held the first workshop in Anaheim, CA, June 2001[1], the second one in Orlando, FL, June 2003[2,3] and the third workshop has been announced to be held in San Francisco, CA, June 2006[2]. The objectives of the workshops are to assess the state-of-the-art computational methods as practical aerodynamic tools for aircraft force and moment prediction of increasingly complex geometries and to identify areas needing additional research and development.

The geometry selected for the second workshop activity was a transonic wing-body transport configuration with nacelles on and off. It is referred to as DLR-F6 model. To maintain as much uniformity among various computations as possible, several baseline multi-block structured, overset, and unstructured grids were generated by the workshop organizing committee and provided to the participants to perform their required computations.

접수일: 2005년 8월 31일, 심사완료일: 2005년 10월 26일.
1 정회원, 한국해양연구원 해양시스템안전연구소
2 정회원, 한국과학기술원 항공우주공학전공
3 정회원, 한국과학기술원 항공우주공학전공
* Corresponding author E-mail: jhkwon@kaist.ac.kr

Participants were also encouraged to develop their own grid and apply their best practices to perform additional cases. The results generated by the participants including present authors are able to be obtained at web-site[2].

This paper summarizes the results obtained with a parallelized multi-block structured grid Navier-Sotkes solver referred to as KFLOW3D. It has been developed at KAIST for reliable computations on real applications. The robustness of KFLOW3D has been extensively verified by performing flow calculations on the steady/unsteady conditions[4-6] for simpler 2-D/3-D configurations such as airfoils, wings, missiles, etc. than that presented in this paper. Brief description about the numerical methodology implemented in KFLOW3D will be presented in the next section and the emphasis of the paper is placed on the implementation of the k-ω WD+ model and verification by computing the DLR-F6 model. More extended documentation on the numerical implementation are presented in Ref.[5].

2. Grids and Test Cases

The DLR-F6 configuration was chosen as model in the workshop and depicted in Fig. 1 and some part of the surface grids are displayed also. The DLR-F6 configuration represents a twin engine wide body aircraft of Airbus type and is derived from the DLR-F4 and they have been extensively used for numerical analysis[7,8]. Detailed descriptions of the F6 and nacelles are available in Refs.[2,7].

The structured multi-block 1-to-1 matched grids are used for the present calculations. The structured 1-to-1 grids are officially supported by both ICEM-CFD Engineering and Boeing Commercial Airplanes group. The latter were used for the present calculations since it showed better grid quality in the wall orthogonality and smooth variation of the grid spacing than the other structured grid set. A prior study also performed using the both grid sets(the results are not presented in this paper). By single point computations using the ICEM-CFD grid, an acceptable results did not obtained while the results with the Boeing-grid showed sufficient accuracy, especially on the pressure distribution. Results by comprehensive comparative study for both grid sets were presented at the workshop[2].

The first required case by the workshop organizing committee is the single point grid convergence study for the design conditions $M_\infty = 0.75$, $Re_\infty = 3 \times 10^6$ (based on the mean aerodynamic chord=141.2mm), $C_L = 0.5$ with

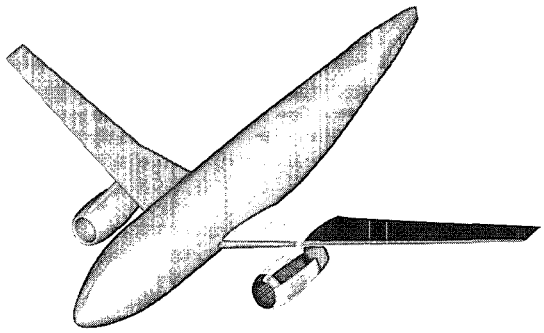

Fig. 1 Geometry of the DLR-F6 configuration

"fully turbulent" solutions using the coarse, medium, and fine grids for wing-body(WB) and wing-body-nacelle-pylon (WBNP) configurations. For the WB configuration, all of the three grids were provided but only medium grid for the WBNP configuration was provided by the Boeing commercial Airplane group because they failed to obtain reasonable solutions using the finer grids[2,3]. Therefore, the single point grid convergence study was carried out for the WB configuration only.

Brief statistics of the grids used in this study are summarized in Table. 1, where WBC, WBM, WBF mean coarse, medium, fine grid for the WB configuration, respectively. The 'N' means total number of grid points, 'BL-MGR' denotes the boundary layer grid maximum growth rate and 'BL cell' means averaged number of cell in the boundary layer. '# of CPU' and 'WTIME' mean the number of CPU and averaged wall-clock time(in hours) for the present calculations, respectively.

The second required case is to obtain the drag polar for angles of attack α_∞= -3° ,-2° ,-1.5° ,0° ,1° ,1.5° for prescribed boundary layer transition location using the

Table. 1 Statistics of the grid systems

	N (Million)	y^+	BL-MGR	BL cell	# of CPU	WTIME
WBC	~ 2.0	~ 1.25	1.40-1.55	18	22	6
WBM	~ 3.7	~ 1.0	1.17-1.24	36	22	12
WBF	~ 13.0	~ 0.8	1.17-1.24	36	58	8
WBNP	~ 5.8	~ 1.0	1.17-1.24	36	20	16

medium grid for both configurations. All computations presented in this paper were carried out in the "fully-turbulent" mode since specification on the boundary layer transition location not yet implemented in KFLOW3D and it is planned to do in the future. Grid resolution study for the second required case has been carried out also using the grids listed in Table. 1 for the WB configuration.

The(optional) drag rise study for various Mach number M_∞=0.50, 0.60, 0.70, 0.72, 0.74, 0.75, 0.76, 0.77 with C_L=0.5 has been performed with the medium grids for both configurations.

3. NUMERICAL METHODS

KFLOW3D, which is still under development, has been developed for the solution of the Reynolds-averaged Navier-Stokes equations. It is a finite-volume cell-center based solver on the multi-block structured grid. It also supports parallel computation using the MPI[9] with the domain decomposition method.

The discretization of the convective fluxes has been realized with upwind schemes such as the 2nd- and 3rd-order MUSCL schemes, 2nd-order upwind TVD scheme[10] using the Roe-FDS[11] with the Harten's entropy fix function[12]. HLLE+[13] scheme is also implemented. In this study, the 3rd-order MUSCL scheme with van Albada limiter is used. The viscous fluxes are discretized using central differences and time integration to steady state is accomplished with the diagonalized ADI(DADI) scheme[14-16]. For convergence acceleration, the local time stepping and the multigrid method with full approximation scheme are used with the V(1,0) cycle and V(1,1) cycle available optionally.

The convergence criteria imposed in this study are as follows: The iteration was terminated when the normalized residual(by that of the first iteration) becomes less than 1×10^{-5} for the given angle of attack cases. For given lift coefficients cases, it was terminated when $\Delta C_L = |C_L - C_{L_{target}}|$ is less than 1×10^{-3} for 1,000 consecutive iterations.

One- and two-equation turbulence models have been implemented. The Spalart-Allmaras(S-A)[17] model and three k-ω turbulence models using linear and non-linear turbulent eddy viscosity models(Wilcox's k-ω[18], Menter's k-ω SST[19] and the weakly non-linear Wilcox -Durbin(WD+)[20]) are implemented in an implicit multigrid context[21]. Detailed description of the comparative study on the three k-ω turbulence models are available in Ref.[5,21]. In this study, the k-ω WD+ model among them is used since it has been found that the non-linear eddy viscosity models improve the performance of turbulence models for flows in presence of adverse pressure gradients, especially in shock- wave/boundary-layer interaction. More comprehensive study on the turbulence models is ongoing now.

4. IMPLEMENTATION OF THE TURBULENCE MODELS

An important requirement in solving the Reynolds-avergaged Navier-Stokes equations is the robustness and efficiency of the solution method. Two-equation turbulence models inevitably have stiff source terms and use very small grid size to resolve thin boundary layer in high Reynolds number flows. This may cause a difficulty in stability and convergence. Some efforts using multigrid method have been devoted to accelerate the convergence of two-equation turbulence models[22-24]. There are several difficulties in implementation of the turbulence transport equations in the multigrid framework. To stabilize the computations one may solve the turbulence transport equations only on the finest grid. However, this may cause slow-down of convergence rates because of disparity between flow and turbulence variables in the coarser grids. To improve the convergence rate with multigrid in the high Reynolds number turbulent flow, it is important to solve the turbulence transport equations at coarser grids. Next, care is needed in the limiting process for preserving positivity of k and ω. Even though implicit treatment of the stiff source terms guarantees positivity of the turbulence variables under certain conditions, the numerical conditions may lead to unphysical values of turbulence variables. In this work, the eddy viscosity and production terms are frozen in coarser grids by passing down the values without a new calculation[24]. Necessary limits are also introduced to avoid this situations.

The turbulent transport equations of the k-ω model can be expressed as follows:

$$\frac{\partial q_T}{\partial t} + \frac{(\partial f_{T_j} - f_{T_{vj}})}{\partial x_j} = S_{kw} \tag{1}$$

where $q_T = [\rho k, \rho\omega]^T$ and

$$f_{Tj} = \begin{bmatrix} \rho u_j k \\ \rho u_j \omega \end{bmatrix}, \quad f_{Tvj} = \begin{bmatrix} (\mu_l + \sigma_k \mu_t)\dfrac{\partial k}{\partial x_j} \\ (\mu_l + \sigma_k \mu_t)\dfrac{\partial \omega}{\partial x_j} \end{bmatrix} \tag{2}$$

where $S_{k\omega}$ is the turbulent source vector. The source vector is composed of the production rates of k and ω, denoted by P_k and P_ω. The eddy viscosity μ_t depends only on turbulent scales:

$$\mu_t = \rho c_\mu \frac{k}{\omega} \tag{3}$$

Original k-ω model[17]

$$S_{org} = \begin{bmatrix} P_k - D_k \\ P_\omega - D_\omega \end{bmatrix} = \begin{bmatrix} \mu_t S^2 - \frac{2}{3}\rho k S_{kk} - \beta^* \rho k\omega \\ \alpha \frac{\omega}{k}\left(\mu_t \frac{S^2}{\alpha_v} - \frac{2}{3}\rho k S_{kk}\right) - \beta\rho\omega^2 \end{bmatrix} \tag{4}$$

where the mean strain rate is defined by

$$S^2 = 2S_{ij}S_{ji} - \frac{2}{3}S_{kk}^2 \tag{5}$$

The closure constants are $\sigma_k = \sigma_\omega = 0.5$, $\beta^* = 1$, $\alpha = 5/9$, $\beta = 5/6$, and $\alpha_v = 1$. The original k-ω model uses a constant value of $c_\mu^* = 0.09$ in the eddy viscosity.

$$\mu_t = \rho c_\mu^* \frac{k}{\omega} \tag{6}$$

The linear eddy viscosity model of Eq. (6) was designed to predict the boundary-layer flows accurately with zero pressure gradient.

k-ω Wilcox-Durbin+(WD+) model[20]

The linear eddy viscosity is known to be inadequated in presence of adverse pressure gradients. Bradshaw[25] pointed out that the shear stress is proportional to the turbulent kinetic energy but not to the velocity gradient in a two-dimensional boundary layer:

$$\tau^* = -\rho\overline{uv} = \rho\sqrt{c_\mu^*}\,k \tag{7}$$

Both expression of Eqs. (6) and (7) can be combined by a functional:

$$c_\mu = \min\left[c_\mu^*, \frac{\sqrt{c_\mu^*}\,\omega}{S}\right] \tag{8}$$

This combination was proposed by Coakley[26] and applied to the k-ω SST model[19] later. This weakly non-linear correction is also fundamentally identical to Durbin's realizability correction[27]. The essential point of the correction is to produce the asymptotic behavior of c_μ when the mean strain rate S tends toward infinity such as the zone in the turbulent boundary layer with adverse pressure gradient or strong thin shear layer. More detailed discussion is found in Ref.[20]. In this work, more elaborate expression of c_μ is used to account three-dimensional effects[28]:

$$c_\mu = \min\left[c_\mu^*, \frac{\sqrt{c_\mu^*}\,\omega}{\sqrt{(S^2+\Omega^2)/2}}\right] \tag{9}$$

If α_v is set to c_μ/c_μ^*, the source vector of the WD+ model is the same to Eq. (4). Other closure constants are the same to those of the original k-ω model.

Time Integration

For k-ω turbulence equations, the source vector of Eq. (4) must be implicitly treated since it results in the stiffness problem of time marching methods. While S^2 term is explicitly treated, the contributions of the turbulent dissipation terms, D_k and D_ω, are added in the implicit parts to increase the diagonal dominance[23]. Therefore, the approximate Jacobian of the source terms can be expressed as:

$$W = \frac{1}{J}\begin{bmatrix} -\widetilde{S_{kk}} - 2\beta\omega & 0 \\ 0 & -\widetilde{S_{kk}} - 2\beta\omega \end{bmatrix} \tag{10}$$

where, $\widetilde{S_{kk}} = Max(0, \frac{2}{3}S_{kk})$. The resulting scheme for each turbulence equation becomes only a scalar ADI method and it is similar with the DADI algorithm used for the Navier-Stokes equations but the estimated spectral radii are used.

$$r^t(A_v) = 2\frac{(\mu_l + \sigma_k\mu_t)}{\rho} \tag{11}$$

Albeit the implicit treatment of the source term greatly improves the robustness involved with the positivity of the turbulence variables, the ω equation can not preserve the positivity constantly. This causes unphysically low level of ω resulting in larger values of eddy viscosity, μ_t. Following Zheng and Liu[22], a lower limit for ω is imposed for every iteration after the turbulence equations are solved:

$$(\rho\omega)_{\min} = \alpha\rho S \tag{12}$$

Multigrid Method

Multigrid method for the turbulence equations requires careful approach because of their high stiffness which results from the non-linear source terms. It has been noted that the strongly non-linear terms can not preserve the accuracy in the coarse levels since the velocity gradients can alter the magnitude of the source terms largely. As such it is important to freeze the non-linear terms in order to preserve the turbulence variables in the coarse levels[23,24]. S^2 and S_{kk} terms are calculated only on the finest grid and restricted as the frozen values to coarser grids:

$$(S^2)_{2h} = \Sigma V_h (S^2)_h / V_{2h} \tag{13}$$

$$(S_{kk})_{2h} = \Sigma V_h (S_{kk})_h / V_{2h} \tag{14}$$

where the subscript h, $2h$ mean the finer grids and coaser grids, respectively and V denotes the cell volume.

Another modification for the multigrid lies on the limiting process. It has been known that the limit for ω, Eq. (12), hinders the effectiveness of multigrid when it is directly imposed at every time step in the coarse grids[23]. Our numerical experiments, however, show a direct imposition of the limit do not counteract the efficiency of the present implicit multigrid method. Therefore, the limiting for ω is directly imposed on all grid levels in this study.

5. RESULTS AND DISCUSSIONS

5.1 EXPERIMENTS[2,3,7]

The design cruise Mach number is $M_\infty = 0.75$ and the lift coefficient $C_L = 0.5$. The aspect ratio is $\Lambda = 9.5$ and the leading edge sweep back angle is $\Phi = 27.1^\circ$. The F6 model was sting mounted in $1.77m \times 1.75m$ transonic test section. Pressure distributions are measured by 288 taps located in 8 spanwise wing sections and 47 locations in 3 radial sections of the nacelle. The Mach number was varied between M_∞=0.6 and 0.8 and the Reynolds number based on the mean aerodynamic chord was kept constant at $Re = 3 \times 10^6$. In each test campaign wing-fuselage measurements had been included for reference purposes. Fig. 2 shows the surface pressure distribution of the configuration by the present calculation at the design cruise condition.

5.2 GRID CONVERGENCE STUDY

A grid convergence study has been performed using the grids listed in Table. 1 for the WB configuration only. Results are shown in Fig. 3. C_D is plotted against $N^{-2/3}$, where N is the total number of grid cells. We can see that the number of cells for the three grid systems were carefully chosen for the grid convergence study with the second-order spatial discretization schemes as shown in Fig. 3. For a second order spatially-accurate scheme, this plot yields nearly linear variation in both $N^{-2/3}$ and C_D. The difference in C_D's to the experimental data(0.0295) lies within 10 counts(coarse: 0.02876, medium: 0.02888, fine: 0.02912). The extrapolated drag coefficient value to an infinite-density predicts the value only 2 counts less than the experimental data.

For the WBNP configuration, the result using the grid shown in Table. 1 is $C_D = 0.03444$, which

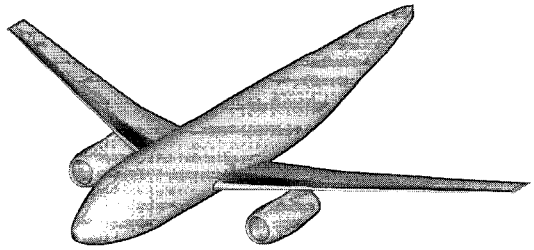

Fig. 2 Surface pressure distribution of the DLR-F6 configuration

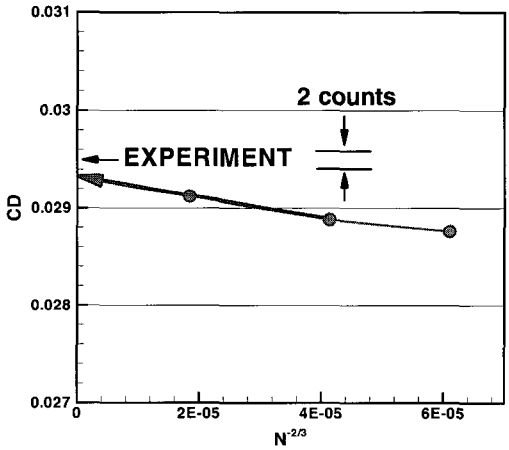

Fig. 3 Grid convergence study for the wing-body configuration

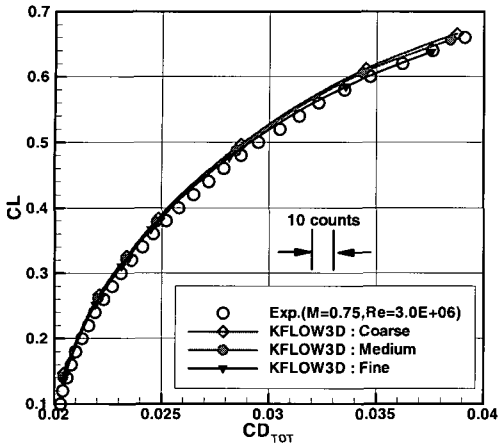

Fig. 4 Drag polar of the wing-body configuration

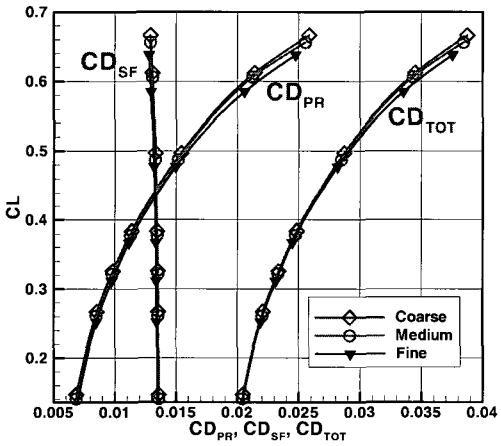

Fig. 5 Lift coefficient vs. pressure-, viscous- and total drag coefficients of the wing-body configuration

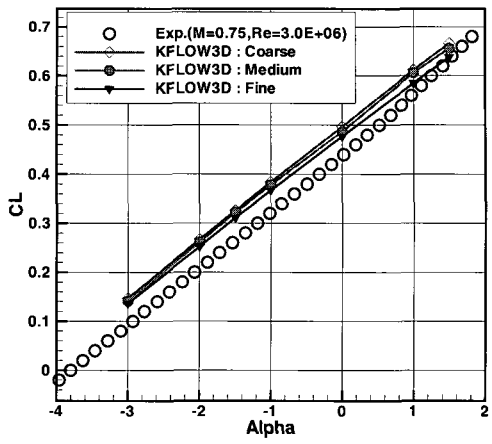

Fig. 6 Lift coefficients vs. angle of attack for the wing-body configuration

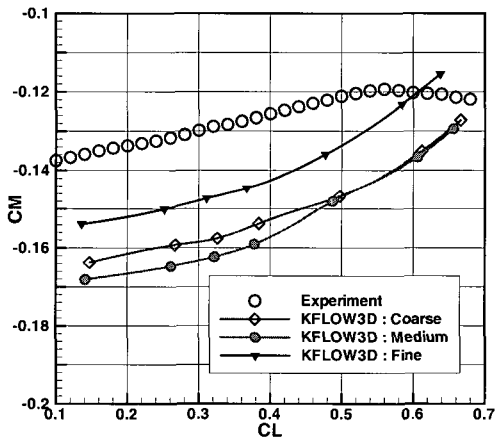

Fig. 7 Moment coefficients vs. lift coefficients of the wing- body configuration

shows only 6 counts difference to the experimental data ($C_{D_{exp}} = 0.0338$).

5.3 Drag polar

The drag polar of the WB configuration are displayed in Fig. 4 and 5 using the three grid sets listed in Table. 1. The results using the present method show very good agreement with the experimental data as shown in Fig. 4, which shows closer to the experimental data as the grid density increases. Fig. 4 shows the drag polars and the pressure- and viscous- components of drag coefficients. The viscous drag components show little variation against the angle of attack.

Fig. 6 displays the lift coefficients with the angle of attacks. Although the difference becomes smaller as the grid density increases, the lift coefficients obtained slightly over-predict than the experimental data that was common aspect for all participants in the workshop-independent on the turbulent models applied and turbulent transition and the grid system (structured multi-block, overlaps, unstructured grid). It was not cleared out by the present authors and all the participants in the workshop.

The moment coefficients versus the lift coefficients are displayed in Fig. 7. For the fine grid, moment coefficients show closer to the experimental data than the other grids.

The drag polar for the WBNP configuration is

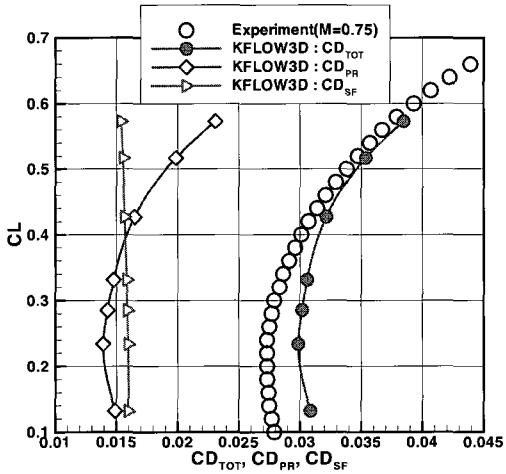

Fig. 8 Drag polar of the wing-body-nacelle-pylon configuration

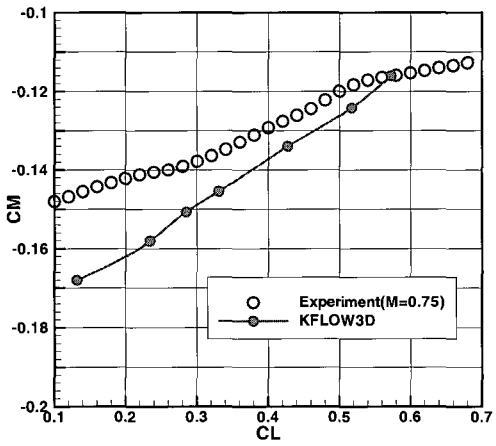

Fig. 10 Moment coefficient vs. lift coefficient of the wing-body-nacelle-pylon configuration

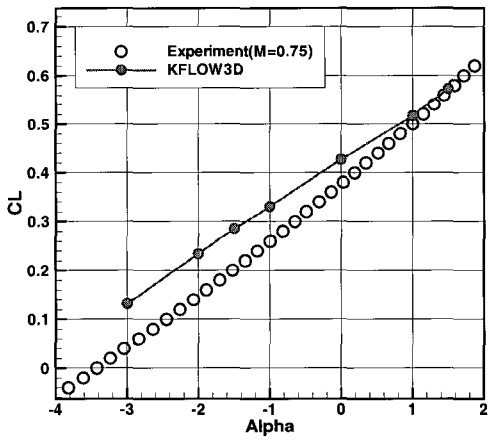

Fig. 9 Lift coefficient vs. angle of attack of the wing-body-nacelle-pylon configuration

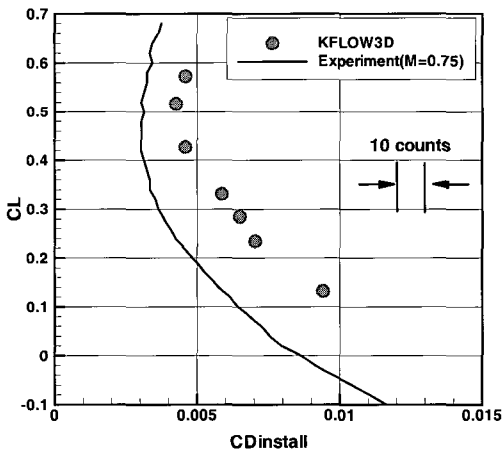

Fig. 11 Installation drag coefficients

displayed in Fig. 8, which shows pressure- and viscous-components also. For this configuration, the drag polar obtained shows shifted aspect to right while those for the WB configuration(Fig. 4,5) slightly shifted to the left compared to the experimental data. The maximum difference between the present result and experimental data is about 40 counts. As shown in Fig. 9, the lift coefficients for the given angle of attack over-predict than the experimental data for this configuration also. The moment coefficients versus the lift coefficients are displayed in Fig. 10.

Based on these data(Fig. 4 and 8) and the value for nacelle internal drag which was measured in calibration tests ($C_{D_{internal}} = 5 \times 10^{-4}$ for $M_\infty = 0.75$) the installation drag can be evaluated using Eq. (15)[7].

$$C_{D_{install}} = C_{D_{wbnp}} - C_{D_{wb}} - C_{D_{internall}} \quad (15)$$

Fig. 11 shows the installation drag obtained by the present computations and experimental data. The maximum discrepancy reaches 34 counts. For the WB configuration, it shows simpler physical phenomena than the WBNP configuration and the drag data has been verified by more rigorous grid convergence study than the WNBP case. It can be trusted, therefore, that the drag polar data of the WB case is more accurate than the other case so that the discrepancy in the WBNP case yields the difference in the installation drag. It will be worthwhile to perform more

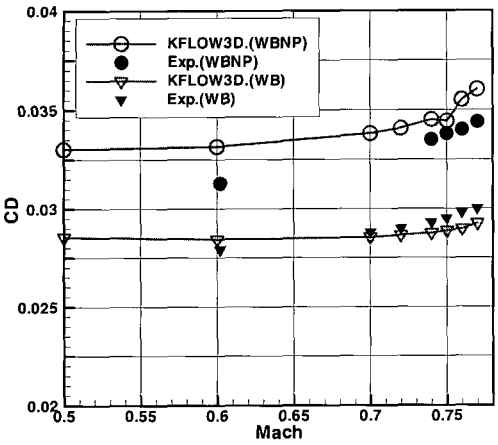

Fig. 12 Drag coefficients vs. Mach number

rigorous verification and validation on the WBNP configuration prior to evaluate installation drag coefficients.

5.4 Drag Rise

Fig. 12 displays the drag rise curves obtained by the present computations and experimental data for both configurations. The present computations show little variation in the drag coefficients in the region where the Mach number is less than 0.7 while the experimental data show larger variation than the numerical data for both configurations. The present computations under-predict the drag coefficient for the WB configuration while they over-predict for the WBNP configuration than the experimental data. In the WB configuration, the present calculations under-predict the drag coefficients for the given lift coefficients as shown in Fig. 4. In the WBNP configuration, the present calculations over-predict the drag coefficients for the given lift coefficients, which is displayed in Fig. 8.

5.5 Pressure Distributions

Investigation on the pressure distribution is also important as well as study on the integrated quantity such as lift, drag, and moment since the integrated quantity might mask the erroneous results so that misleading conclusion can be induced. It has been performed to verify consistency between pressure field obtained by the present calculations and the integrated aerodynamic coefficients discussed above since it is well known that the contribution of the pressure force to the lift force is much larger than the contribution of the viscous force.

The experimental conditions are α_∞=0.49°, C_L=0.4984, M_∞=0.75 and Re_∞=3×10^6. The first comparison of the pressure distribution for the given angle of attack α_∞=0.49° has been performed by using a family of successively finergrids for the WB configuration. Fig. 13 displays the surface pressure distributions at selected spanwise sections $\eta(=2y/b)$=0.239, 0.331, and 0.638. The results by using three grids show little difference except the shock wave resolution and very goodagreement with the experimental data.

The second comparison of the pressure distribution was performed for the given angle of attack α_∞=0.49° and for the given lift coefficient C_L=0.5 by using the fine grid discussed above. The results for the given angle of attack case show better agreement with experimental data than the results for the given lift coefficient as shown in Fig. 14 Results for the given lift coefficients predict lower leading edge suction-roof and weaker shock wave strength than the experimental data on the upper surface and show little disparity with the experimental data on the lower surface. The contribution of the pressure distributions to the lift force is slightly larger than the experimental data for the given angle of attack. It seems that this difference yields over-prediction of the lift coefficient for the given angle of attack as shown in Fig. 6.

The next comparison, the surface pressure distributions at the wing sections of the WBNP configuration are displayed in Fig. 14. The experimental conditions for this case are M_∞=0.75, Re_∞=3×10^6, the angle of attack α_∞ =1° and the lift coefficient C_L=0.4981. Numerical computations are performed for both angle of attack(α_∞ =1°) and lift coefficient(C_L=0.5) to compare the results with the experimental data. The pressure distributions at pylon inboard section($\eta(=2y/b)$=0.331) show the shock wave on both lower and upper surface of the wing and separation on the upper surface of the wing due to the strong shock wave. The results by the present computation with the given angle of attack show better agreement with the experimental data than that with the given lift coefficients especially about the shock wave.

As the last comparison, Fig. 16 shows the surface pressure distribution on the nacelle surface. Fig. 16(a) display the pressure tab location on the nacelle surface in the experiments. The pressure distribution computed and experimental data are shown in Fig. 16(b) and Fig. 16(c) which are inboard side and outboard side, respectively. On the nacelle surface, the results for both computational conditions show little difference.

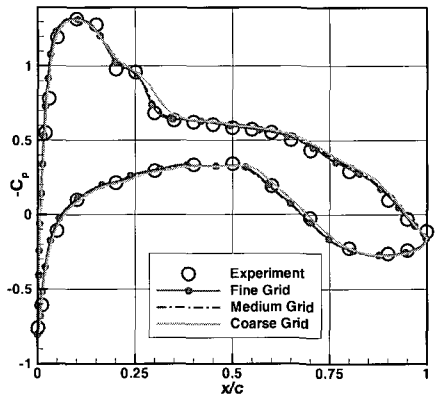

(a) η = 0.239

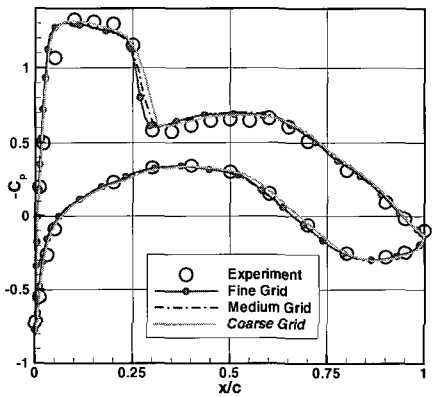

(b) η = 0.331

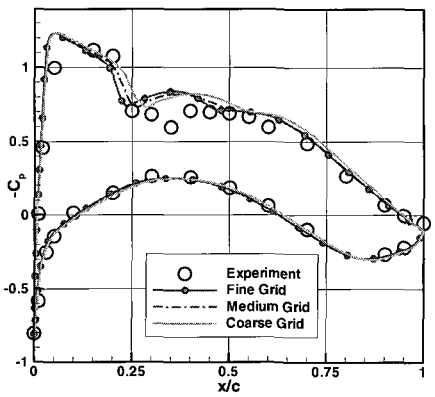

(c) η = 0.638

Fig. 13 Pressure distributions of the wing-body configuration (α = 0.49°)

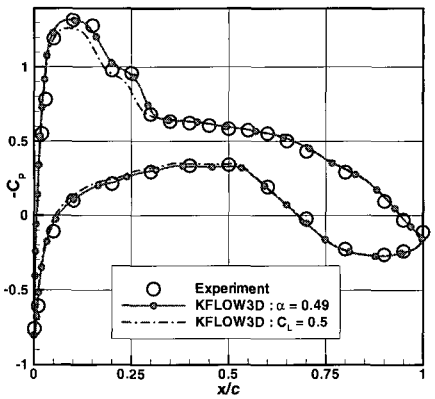

(a) η = 0.239

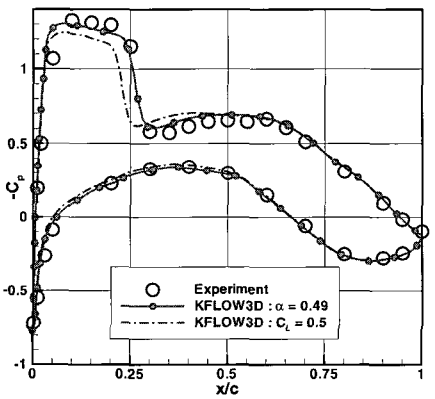

(b) η = 0.331

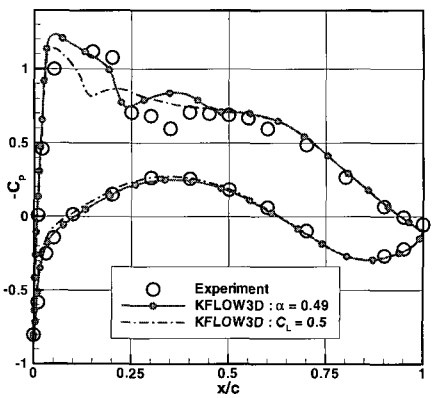

(c) η = 0.638

Fig. 14 Pressure distributions of the wing-body configuration (α = 0.49° and C_L = 0.5) for fine grid

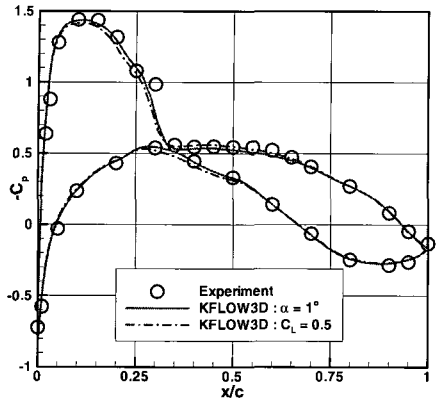

(a) η = 0.239

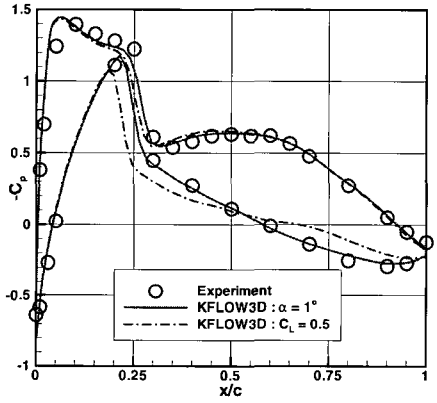

(b) η = 0.331

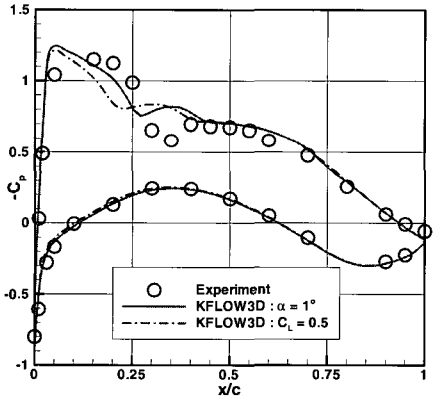

(c) η = 0.638

Fig. 15 Pressure distributions on the wing surface of the wing-body-nacelle-pylon configuration

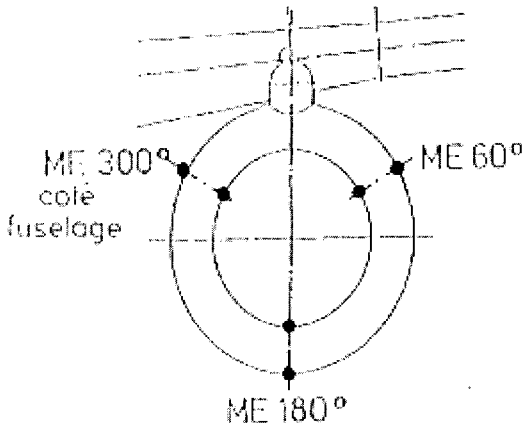

(a) Pressure tab locations on the nacelle

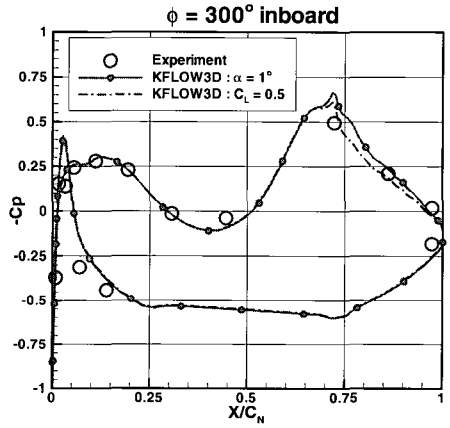

(b) ϕ= 300° inboard side

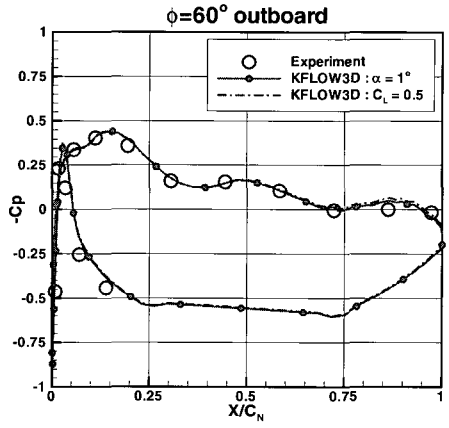

(c) ϕ= 60° outboard side

Fig. 16 Surface pressure distribution on the nacelle surface of the wing-body-nacelle-pylon configuration

6. CONCLUDING REMARKS

A parallelized 3-D compressible Navier-Stokes solver KFLOW3D has been developed and its robustness has been verified by performing the turbulent flow simulations about the DLR-F6 WB and WBNP configurations. Two-equation k-ω WD+ turbulence model is implemented and it provides very good results for the DLR-F6 configurations due to its merits on the transonic separated flows[21]. Especially, the KFLOW3D predicts very accurate drag coefficients in the grid convergence study and surface pressure distributions compared to the experimental data.

It will be worthwhile to perform more rigorous and systematic approach for quantifying the uncertainty in the numerical simulations prior to calculation of integrated aerodynamic coefficients for complex geometry with complex physical phenomena. It is encouraging news to be held the third workshop next year, and it is trusted to assess the state-of-the-art of the CFD code more rigorously.

ACKNOWLEDGEMENTS

This work was partially supported by the "Dual Use Technology Program" of the MOCIE.

REFERENCES

[1] Levy, D.W., Zickuhr, T., Vassberg, J., Agrawal, S., Wahls, R.A., Pirzadeh, S.Z., and Hemsch, M.J., 2002, "Summary of Data from the First AIAA CFD Drag Prediction Workshop," *AIAA* Paper 2002-0841.

[2] http://aaac.larc.nasa.gov/tsab/cfdlarc/aiaa-dpw/

[3] Laflin, K.R. et al, 2004, "Summary of Data from the Second AIAA CFD Drag Prediction Workshop," *AIAA* Paper 2004-0555.

[4] Park, S.H., Kim, Y., and Kwon, J.H., 2003, "Prediction of Damping Coefficients Using the Unsteady Euler Equations," *J. of Spacecraft and Rockets*, Vol.40, No.3, p.356-362.

[5] Park, S.H., and Kwon, J.H., 2004, "Implementation of k-ω Turbulence Models in an Implicit Multigrid Method," *AIAA J.*, Vol.42, No.7, p.1348-1357.

[6] Park, S.H., and Kwon, J.H., 2003, "Comparisons of Steady and Unsteady Methods for Pitch-Damping Predictions," *AIAA* Paper 2003-3671.

[7] Brodersen, O., and Sturmer, A., 2001, "Drag Prediction of Engine-Airframe Interference Effects Using Unstructured Navier-Stokes Calculations," *AIAA* Paper 2001-2414.

[8] Redeker, G., 1994, "DLR-F4 Wing-Body Configuration," A Selection of Experimental Test Cases for the Validation of CFD Codes," *AGARD Report* AR-303.

[9] Gropp, W. *et al*, 1999, "*MPI - The Complet Reference*," *The MIT Press*.

[10] Park, T.S., and Kwon, J.H., 1996, "An Improved Multistage Time Stepping for Second-Order Upwind TVD Schemes," *Computers and Fluids*, Vol.25, No.7, p.629-645.

[11] Roe, P.L., 1981, "Approximate Riemann Solver, Parameter Vectors and Difference Schemes," *J. of Comput. Phys.*, Vol.43, No.2, p.357-372.

[12] Harten, A., 1983, "High Resolution Schemes for Hyperbolic Conservation Laws," *J. of Comput. Phys.*, Vol.49, p.357-393.

[13] Park, S.H., and Kwon, J.H., 2003, "On the Dissipation Mechanism of Godunov-Type Schemes," *J. of Comput. Phys.*, Vol.188, No.2, p.524-542.

[14] Sung, C.H., Park, S.H., and Kwon, J.H., 2001, "Multigrid Diagonalized ADI Method for Compressible Flows," *AIAA* Paper 2001-2556.

[15] Pulliam, T.H., and Chaussee, D.S., 1981, "A Diagonal Form of an Implicit Approximate-Factorization Algorithm," *J. of Comput. Phys.*, Vol.39, p.347-363.

[16] Caughey, D.A., 1988, "Diagonal Implicit Multigrid Algorithm for the Euler Equations," *AIAA J.*, Vol.26, No.7, p.841-851.

[17] Spalart, P.R., and Allmaras, S.R., 1992, "A One-Equation Turbulence Model for Aerodynamic Flows," *AIAA* Paper 92-0439.

[18] Wilcox, D.C., 1988, "Reassessment of the Scale-Determining Equation for Advanced Turbulence Models," *AIAA J.*, Vol.26, No.11, p.1299-1310.

[19] Menter, F.R., 1994, "Two-Equation Eddy-Viscosity Turbulence Models for Engineering Applications," *AIAA J.*, Vol.32, No.8, p.1598-1605.

[20] Thivet, F., 2002, "Lessons Learned from RANS Simulations of Shock-Wave/Boundary-Layer Interactions," *AIAA* Paper 2002-0583.

[21] Park, S.H., and Kwon, J.H., 2003, "Comparative Study of k-ω Turbulence Models for Transonic Separated Flows," *Proceedings of the Fifth Asian Computational Fluid Dynamics Conference*, Busan, Korea.

[22] Zheng, X., and Liu, F., 1995, "Staggered Upwind Method for Solving Navier-Stokes and k-ω Turbulence

Model Equations," *AIAA J.*, Vol.33, No.6, p.991-998.
[23] Liu, F., and Zheng, X., 1996, "A Strongly Coupled Time-Marching Method for Solving the Navier-Stokes and k-ω Turbulence Model Equations with Multigrid," *J. of Comput. Phys.*, Vol.128, No.2, p.289-300.
[24] Gerlinger, P., and Bruggemann, D., 1997, "Multigrid Convergence Acceleration for Turbulent Supersonic Flows," *Int. J. for Numerical Methods in Fluids,* Vol.24, No.10, p.1019-1035.
[25] Bradshaw, P., Ferriss, D.H., and Atwell, N.P., 1967, "Calculation of Boundary-Layer Development Using the Turbulent Energy Equation," *J. of Fluid Mechanics*, Vol.28, No.3, p.593-616.
[26] Coakley, T.J., 1983, "Turbulence Modeling Methods for the Compressible Navier-Stokes Equations," *AIAA* Paper 83-1693.
[27] Durbin, P.A., 1996, "On the k-ε Stagnation Point Anomaly," *Int. J. of Heat and Fluid Flow*, Vol.17, No.1, p.89-90.
[28] Moore, J.G., and Moore, J., 1999, "Realizability in Two-Equation Turbulence Models," *AIAA* Paper 99-3779.